

An assessment of potential wave power along a coastal province, Central Vietnam

Tran T. Tung and Nguyen Q. Chien

Abstract— The potential wave power has been assessed based on long-term wave data along a marginal sea area offshore Phu Yen province in Central Vietnam. Based on the publicly available WaveWatch-III reanalysis wave data (NOAA), the deep-water wave climate during the period from 1989 to 2019 has been analysed and used as the boundary condition for the MIKE21 spectral wave model. The hydrodynamic module of MIKE21 is also run in coupled mode. The model has been calibrated and verified against the measured data at three wave gauges. Simulation has been performed for every month, each with 1-2 typical wave conditions. The results show that the highest wave power (~29 kW/m) occurs in December. The distribution of wave power along the 30-m depth contour has also been presented for the annual average, NE monsoon (winter) average, and S monsoon (summer) average. The distribution map shows that wave power is slightly higher in the south of this area, and the NE monsoon season comes along with much higher wave power (7.4 times compared to that of the S monsoon season). These findings may aid in planning the effective exploitation of wave energy for the region.

Keywords— monsoon season, ocean wave power, Vietnam coast, wave energy converter, wave modelling

I. INTRODUCTION

THE potential of ocean wave energy has been internationally recognised [1]–[3]. By the 1970s, developed countries such as the USA, Japan, UK, Scandinavian countries, and India began to research and utilise this energy type. Since 2000, commercial devices

such as Wave Dragon [4] and Pelamis [5] have been widely used. In particular, for EU countries (and the UK), where policies encourage the use of renewable energies, wave energy converters (WECs) are connected to power networks and represent an essential contribution to national energy security [6]. Various types of WECs have been applied [7], [8], and their reliability and design aspects were assessed based on survival and design response analysis [9].

An often-used method in assessing the wave energy potential of the deep-sea regions where WECs are designed to operate is to collect measured wave data from nearby oceanographic gauges. A scatter plot between the significant wave height and the wave period is made [10], which shows the possibility of exploiting high-energy wave conditions from a specific sea region in the long term.

From wave data series obtained from oceanographic stations, it is also possible to determine the maximum, minimum, and average wave energy in a given time period. In addition, maps of the annually-, seasonally- and monthly-averaged wave energy can be drawn. Such maps had been made for the global oceans [11], the Mediterranean Sea [12], the Black Sea [13], the East China Sea and South China Sea [14], the South China Sea [15], and the northern Indian Ocean [16].

The use of remotely sensed data is also prevalent. Norway established a wave energy map for its western coast during the months Sep-Nov, from satellite-derived data. The data points are 20-50 km apart in the deep-water zone and more densely spaced in the nearshore zone. A map of sea regions of Western Europe was made in terms of the annual average and total wave energy [6].

By taking advantage of the increasing capability of computers, recent studies have performed wave simulations based on available wave datasets. These numerical simulations are powerful as they provide crucial wave properties to estimate the wave power in a high spatial resolution. For example, Kamranzad and Lin [17] used the spectral wave model SWAN to model the long-term variation of wave power in the South China Sea for 55 years. The model has a spatial resolution of $0.25^\circ \times 0.25^\circ$ and a temporal resolution of 30 mins. Rusu [18] also used SWAN but was restricted to modelling

Manuscript received 13 April; accepted 8 December 2022; published 31 March 2023.

This is an open access article distributed under the terms of the Creative Commons Attribution 4.0 licence (CC BY <https://creativecommons.org/licenses/by/4.0/>). This article has been subject to single-blind peer review by a minimum of two reviewers.

This work was supported in part by the Vietnam government under grant DTDLCN.33/18.

T. T. Tung with Faculty of Civil Engineering, Thuyloi University, 175 Tay Son, Dong Da, Hanoi, Vietnam (e-mail: t.t.tung@tlu.edu.vn).

N. Q. Chien is with Faculty of Civil Engineering, Thuyloi University, Hanoi, Vietnam (e-mail: chien.n.q@tlu.edu.vn); currently as Postdoc Research Assistant at Department of Physics, Aberystwyth University, Ceredigion SY23 3BZ, UK.

Digital Object Identifier: <https://doi.org/10.36688/imej.6.27-35>

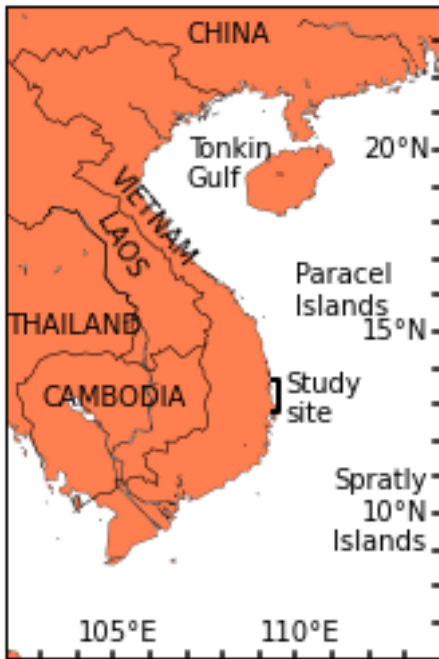


Fig. 1. Location of Phu Yen coast (the study site) in Vietnam

nearshore areas of the Iberian coasts facing the Atlantic Ocean. On the other hand, the resolutions are higher (spatial resolution 0.02° and temporal resolution 10 mins.)

Another trend of research is to evaluate the possibility of energy extraction from nearshore waves, particularly to identify suitable locations to deploy WECs. Behrens et al. [19] assessed the distribution of wave energy along the Australian coast. They compared the efficiency of three types of devices – the point absorber, the terminator, and the linear attenuator. Rusu and Guedes Soares [20] evaluated the ability to extract wave energy with the buoy-type device ‘PELAMIS’ for Azores Islands in the Atlantic Ocean. Mota and Pinto [21] estimated the wave power distribution along the western coast of Portugal and compared three methods to calculate the wave power based on the point location and orientation.

In Vietnam, most of the research projects on wave energy have been conducted recently, since around 2000. The potential of wave power in deep waters and wave energy extraction to serve the regional economy is the main focus of these studies. Nhat et al. [22] studied the application of wave energy in lighting beacons for navigation. Quynh et al. [23] provided an overall view of wave and tidal energy for Vietnam’s coastal areas. They recommended that the Vietnamese coast be divided latitudinally into six zones, based on the wave climate and wave power potential. The Southern-Central Coast has the highest annually-averaged wave power (~ 30 kW/m) due to its exposure to the South China Sea and a narrow continental shelf. Hung and Dien [15] established maps featuring exploitable ocean energy sources (wind, wave, and tide). The maps are based on wave parameters estimated from the SWAN model for the South China Sea

with the satellite-derived JMA wind field as input. The authors indicated that the wave power potential depends directly on the monsoon regime. Again, the South-Central Coast has a high potential offshore wave power, reaching 25 kW/m. More recently, Wang et al. [24] further studied the economic aspect of wave energy extraction for the Vietnam coastline. They used a multiple-criteria decision-making (MCDM) model to find an optimal site among ten alternatives. A contemporary report [24b] compared SWAN simulations (with a 4-km resolution) forced by ERA5 wind field to the ECMWF reanalysis (0.125° resolution) and CMEMS data (0.2°) and showed that the SWAN estimates were generally lower than those of ECMWF; the latter were used for wave resource assessment.

Within this area, the coastal province of Phu Yen (the “study site” in Fig. 1) has a pertinent advantage in multi-sector economic development along its 190-km coastline. Such activity requires an additional power supply, preferably locally generated, for that wave energy is an important renewable source. As mentioned above, previous studies only focused on offshore wave power. Recently, it has been reported [25] that the enclosing central Vietnam coastline has an annually-average wave power of 8 kW/m and is only the nearshore zone of Vietnam with a wave energy potential for extraction. However, in this analysis, local features such as coastline orientation were not considered. Therefore, a detailed assessment of the wave power for the Phu Yen coast is necessary.

In this paper, the long-term average wave power distribution along the Phu Yen coast is presented. Specifically, the characteristics of waves during various periods: monthly, annually, and each of the two monsoon seasons is compared. The method to estimate the wave power along the Phu Yen coast is presented in Section II. In Section III, the properties of offshore waves are calculated using the WaveWatch III (WW3) reanalysis data archive [26]. These offshore wave characteristics serve as boundary conditions for the MIKE21 spectral wave model. The model is then set up and validated using measured data (Section IV). The modelling results are presented and discussed in Section V. Finally, conclusions are given in Section VI.

II. ESTIMATING WAVE POWER IN COASTAL WATERS

The wave power in deep water and in arbitrary water depths can be estimated as:

$$P_0 = \frac{\rho g^2}{64\pi} H_s^2 T_e \quad (1)$$

$$P = EC_g \quad (2)$$

where P = wave power for a unit of wave crest length (W/m), P_0 = wave power in deep water, ρ = sea-water density (kg/m³), g = gravitational acceleration (m/s²), H_s = significant wave height (m), T_e = wave energy period (s), E = wave energy density (J/m²) and C_g = wave group velocity.

While the definition of H_s is widely agreed upon, the wave energy period can be defined in several ways. Twidell and Weir [6] considered T_e being equal to the peak period. Saulnier *et al.* [27] considered $T_e = m_{-1}/m_0$, where m_{-1} is the (-1)th moment and m_0 is the 0th-order moment of the wave spectrum. A relationship between T_e and the zero-crossing period, T_z , is $T_e = kT_z$ where $k = 1.1$ to 1.3. Behrens *et al.* [19], on the other hand, recommended: $T_e = 0.86 T_p$.

In practice, signal processing techniques are used to evaluate H_{m0} ($\approx H_s$) and T_e for the design and exploit wave energy potential. In addition, modelling software suites usually provide output for quantities such as E and C_g , from which the wave power field can be calculated from Eq. (2). This field is commonly represented as shaded contours, for example, the South China Sea wave power map [15]. It should be noted that, as random sea waves, in reality, propagates in different directions, the energy is effectively smaller than that calculated from (2).

However, the above calculation method only provided the necessary information for designing point absorber devices. For terminator devices, it is essential to consider the wave power across the terminator route. If the incident wave makes an angle α with the route, the wave power will be $P' = P \cos\alpha$.

Mota and Pinto [21] considered such wave powers, and they mentioned two cases: (a) The route is perpendicular to the annually-averaged wave direction, and (b) The route is parallel to the shoreline but is located in a zone with water depth ~ 50 m. For Case (a), the average wave direction is NW, and the power ranges from 21 kW/m in southern Portugal to 31 kW/m in northern Portugal. For Case (b), the nearshore wave power ranges from 100 to 190 MWh/m/yr (which converts to 11-21 kW/m). Thus, due to the obliqueness of incoming waves related to the shore, the net power received may be lower than that of the annually averaged wave condition.

In this paper, the authors choose a calculation method similar to the Case (b) above, i.e. the route is along the depth contour of 30 m. This particular water depth is chosen to align with the regional coastal management rules, which regulate the spatial extent for the deployment of WECs in the Vietnamese continental shelf. The location of this contour is shown in Fig. 4 as a dashed

TABLE I
MONTHLY TYPICAL WAVE CONDITIONS FOR OFFSHORE PHU YEN COAST

Wave cond.	H_s (m)	T_p (s)	θ (°)	Occ. (%)
Jan, NE	2.42	8.46	51.7	99.7
Feb, NE	2.04	8.14	52.2	94.4
Mar, NE	1.66	7.74	51.7	87.3
Mar, S	0.75	4.19	141.8	12.3
Apr, NE	1.18	7.38	52.5	66.6
Apr, S	0.85	4.21	164.3	32.8
May, NE	1.02	7.16	53.5	38.7
May, S	0.92	4.80	174.2	59.6
Jun, NE	0.84	6.69	56.1	9.5
Jun, S	1.04	5.64	179.5	84.8
Jul, NE	0.93	8.70	59.7	7.4
Jul, S	1.09	5.98	181.3	87.4
Aug, NE	0.95	9.04	55.7	10.5
Aug, S	1.15	6.30	183.5	82.0
Sep, NE	1.17	8.20	63.8	45.7
Sep, S	1.05	6.06	178.5	50.5
Oct, NE	1.89	8.46	47.8	94.9
Nov, NE	2.57	8.79	49.8	99.3
Dec, NE	3.01	9.08	51.3	99.8

curve. It is not parallel to the shoreline: the distance is only ~ 2 km in the southern part of the area but up to ~ 12 km in the northern part.

III. REPRESENTATIVE DEEP-WATER WAVE CONDITION

The typical wave condition comprises the following characteristics: H_s (significant wave height), T_p (peak wave period), and θ (main wave direction). The authors use reanalysis wave data [26] from the WaveWatch III model [28] for boundary conditions. The practice of adopting computed wave conditions from larger models has been done in previous works. For example, Karunaratna *et al.* [29] used the KU_IO model for the Indian Ocean region to generate H_s , T_{m01} and θ for the Sri Lanka domain. The WaveWatch III model had been validated against offshore buoys and satellite altimeters with good results. The wave data spans from 1989 to 2019, with a sampling interval of three hours and a spatial resolution of 0.5 geographical degrees. The details of the data used are missing, such as bathymetry source and resolution wave data (NOAA) resolution. For this study, the wave data is sampled at 110°E, 13.5°N (corresponding to an easting of $X = 1041740$ m and northing of $Y = 1497931$ m in the UTM coordinate system; positioned at the star symbol in Fig. 3). This location is outside the continental shelf and thus experiences deep-water wave conditions. Fig. 2 shows the average annual wave rose for the location.

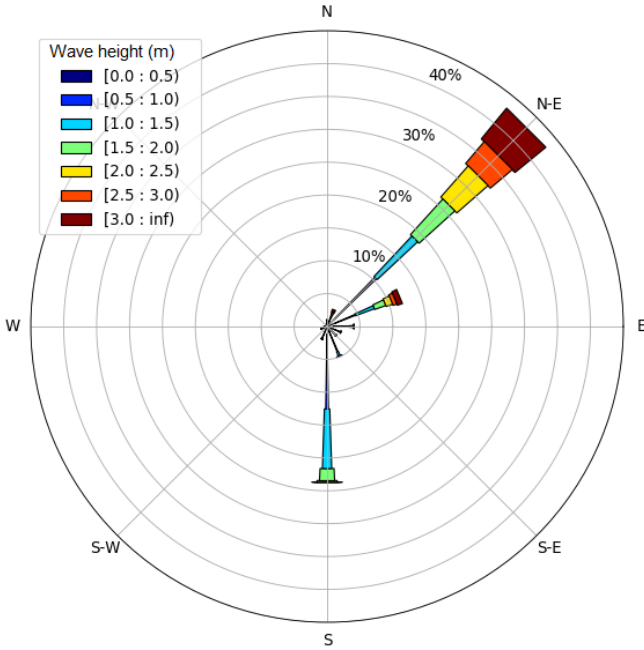


Fig. 2. Long-term wave rose from WAVEWATCH data at sampling location 110°E, 13.5°N [26]

Based on the wave rose, two dominant groups of waves become apparent: NE and S. The criterion for splitting these groups is $\theta_{\text{threshold}} = 101^\circ$ (a direction roughly between E and ESE, which best separates the two groups). For each group, the wave characteristics are calculated following Goda [30]:

$$H = \sqrt{\frac{\sum H_i^2 T_i}{\sum T_i}} \quad (3)$$

$$T = \frac{\sum T_i}{N} \quad (4)$$

$$\theta = \frac{\sum \theta_i H_i^2 T_i}{\sum H_i^2 T_i} \quad (5)$$

where the sum Σ is implemented from 1 to N ; i is the index number of each wave sample, and N is the total number of samples (N ranges from 18 for the NE group in July to 247 for the NE group in December).

The monthly typical wave condition is calculated as in Table 1 (for months from Mar to Sep, each month has two typical conditions). For months Oct-Dec and Jan-Feb, due to the enduring influence of the northeastern monsoon, each month shows only one group of directions (Data Group 1) with a representative angle $\theta_1 \approx 52^\circ$. During Mar-Sep, another group (Data Group 2) also appears with a representative angle $\theta_2 \approx 177^\circ$. The first group has higher waves on average (2.00 m versus 1.03 m of Data Group 2).

Although the wave condition in extreme events such as typhoons is not considered here, this can be justified. First, the effect of typhoons on the seasonal average of the

local wave power should be negligible due to the short duration of such events. Also, the severe conditions during storms and typhoons pose a problem to the survivability of WECs [6]. Therefore, we assume that the WECs are not planned to operate during very high wave conditions.

IV. HYDRODYNAMIC AND WAVE MODELLING

A. Model set-up

The modelling system used is MIKE21 [31], which allows numerical simulation of wave propagation and flow process in coupled mode. The rectangular model domain is aligned with the coastline, which runs almost north-south. The domain spans from $X = 964791$ m to 1019370 m easting and $Y = 1533730$ m to 1403566 m northing. The offshore side of this domain does not reach the wave sampling point mentioned in Section III. However, this side is entirely in the deep-water zone, and waves can propagate from the sampling point to the side without notable distortion in either wave height, wave period or wave direction. An unstructured grid is set up with 7979 nodes and 14165 elements, with the finest grid size of ~ 200 m. This allows adequate resolution of the local coastline features such as bays and headlands in wave modelling. In terms of hydrodynamics, the mesh size Δ imposes a horizontal viscosity K , which represents the parametrisation of turbulence on the sub-grid scale. It can be calculated empirically [32] as $K = 0.001\Delta^4/3$. In bays and nearshore zones, Δ ranges from 1.2 to 4.0 $\text{m}^2 \text{s}^{-1}$. This is appropriate with the recommendation (0.1 to 100 $\text{m}^2 \text{s}^{-1}$) for open waterbodies such as lakes [33] and must be larger than $O(0.1) \text{m}^2 \text{s}^{-1}$ for surf zones [34]. The nearshore bathymetry dataset has been integrated from the nautical chart for deeper waters and surveys of this project (DTDLCN.33/18) with echo sounding in Project DTDL.CN.15/15 (see Section B) for nearshore areas. These elevations are represented in Vietnam National Height Datum.

Three boundaries of the model are specified along the northern, eastern, and southern edges of the domain. For the hydrodynamic boundary condition, the water level time series were obtained from the MIKE21 tidal prediction module DTU10 [35]. For the wave boundary conditions, wave properties, including the significant wave height, peak wave period, and mean wave direction, are retrieved from NOAA's global reanalysis wave data as detailed in Section III.

B. Model calibration and validation

Data for calibrating and verifying the model is provided by a previously conducted research project (Grant DTDL.CN.15/15) "Mechanism of sediment deposition and erosion and stabilisation solutions for Da Dien and Da Nong river mouths" and the current project (DTDLCN.33/18). In the former project, measurements included wave gauging at Locations B (13.078°N ,

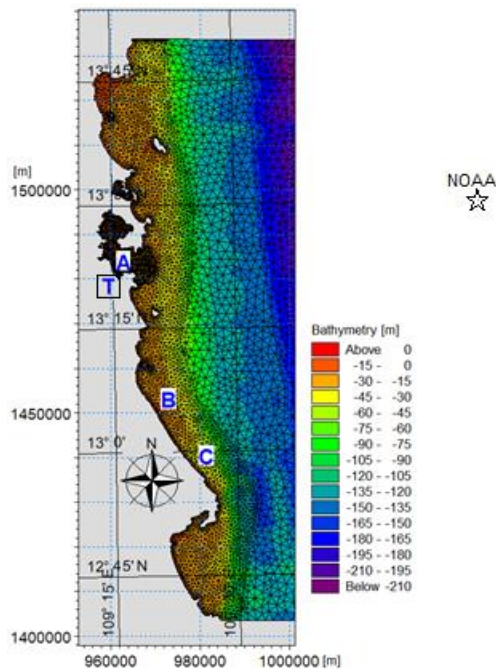


Fig. 3. Computational domain and grid with tidal (T) and wave gauging locations (A, B, C). The location for the NOAA wave data sampling data is also shown as a star symbol.

109.344°E, ~10 m water depth) and C (12.958°N, 109.426°E, ~18 m), as shown in Fig. 3. In the latter project, water level gauging was at Location T and wave gauging at A. Waves were measured using an AWAC device, whereas the water levels were recorded with an EMS WaveLogger pressure sensor-type device. Due to limited time in device deployment in the field surveys, the data were only available for seven days for a typical campaign (5-Jun to 12-Jun-2017, 2-Jun to 9-Jun-2019 and 15-Oct to 22-Oct-2019) except for a longer campaign in which data were recorded during ten days (17-Nov to 27-Nov-2016).

We split the dataset for model calibration and validation as follows:

- Dataset Jun-2019 is used for calibrating water level at T and wave at A; dataset Jun-2017 is used for calibrating waves at B and C;
- Dataset Oct-2019 is used for validating water level at T and wave at A; dataset Nov-2016 is used for validating waves at B and C. During the Nov-2016 campaign, the wave sensor at C yielded a spurious directional signal, which is not consistent with the field condition (NE-dominant waves). Therefore, the wave direction at C is not validated.

By arranging the calibration period in the summer (characterised by wave data group 2) and the validation period in autumn (wave data group 1), we focus on the validation part for the more energetic sea states. This

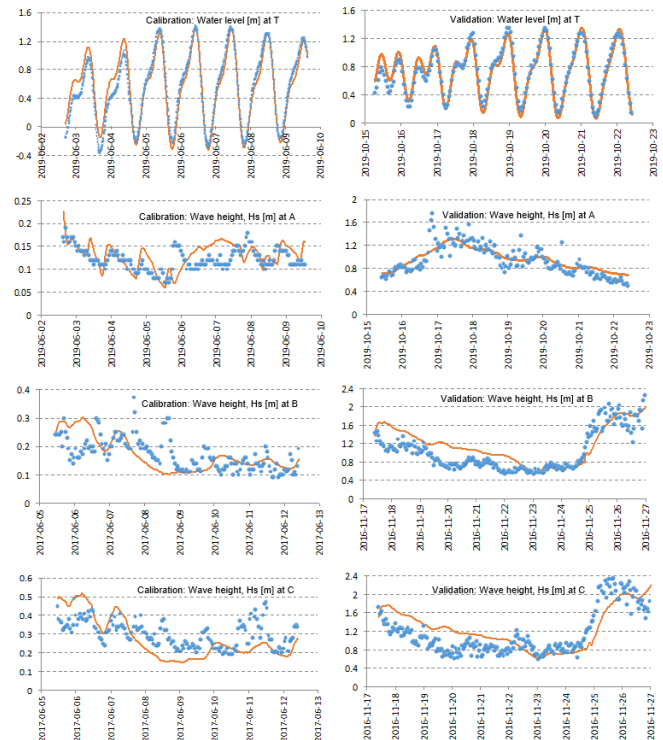


Fig. 4. Calibration and validation results for hydrodynamic (water level at tidal station T) and wave modelling (significant wave height at A, B, and C wave gauges). The solid lines represent computed time series and filled dots denote observed data.

would ensure that the model will operate well for realistic wave conditions.

The model was run for a time step of 60 s. The commonly used JONSWAP wave spectral shape is specified for all open boundaries. The calibration work is taken by first tuning the friction parameters. A Nikuradse roughness of 0.04 m is chosen for the seabed in the wave module, while a Strickler coefficient of 36 $\text{m}^{1/3} \text{s}^{-1}$ is selected for the flow module. Additionally, the horizontal viscosity is parameterised using the Smagorinsky formulation with a coefficient of 0.28. After the water level is appropriately calibrated, we calibrate the wave module by choosing the whitecapping dissipation coefficients C_{dis} as 4.5 and δ_{dis} as 0.5 and setting a breaking wave index to 0.68.

C. Calibration and validation results

The comparison between the simulated and measured data series is shown in Fig. 4 (times are represented in the local time zone, GMT+7). It can be seen that the hydrodynamic model can capture the high and low water levels. The over-predictions in the first two tidal cycles are due to model spin-up). The Nash indices are 0.93 and 0.94 for calibration and validation, respectively. (All errors and performance statistics are presented in Table 2, with their definition listed in Appendix 1.) The relatively high Nash index (> 0.8) allows the tidal hydrodynamic model to be used in the coupled mode for simulating various scenarios described in Section III.

TABLE 2
GOODNESS-OF-FIT FOR WAVE MODEL CALIBRATION AND VALIDATION

Quantity and gauge	Cal MAE	Cal RMSE	Cal Bias	Cal SI	Cal ^a Nash	Cal BSS	Cal <i>r</i>	Val MAE	Val RMSE	Val Bias	Val SI	Val Nash	Val BSS	Val <i>r</i>
WL [T]	9.8 cm	12.4 cm	1.2 cm	0.22	0.93	0.97	0.97	6.6 cm	8.5 cm	0.7 cm	0.12	0.94	0.99	0.97
<i>H_s</i> [A]	2.3 cm	2.9 cm	0.9 cm	0.24	X	0.94	0.43	11.0 cm	14.5 cm	2.3 cm	0.16	X	0.97	0.86
<i>H_s</i> [B]	4.5 cm	6.2 cm	0.0 cm	0.36	X	0.88	0.42	23.1 cm	28.3 cm	14.7 cm	0.28	X	0.93	0.84
<i>H_s</i> [C]	8.0 cm	9.5 cm	-2.6 cm	0.32	X	0.91	0.60	28.2 cm	33.1 cm	9.2 cm	0.29	X	0.93	0.76
<i>T_{m02}</i> [A]	0.53 s	0.64 s	-0.18 s	0.19	X	0.96	0.36	1.31 s	1.44 s	-0.74 s	0.18	X	0.97	0.69
<i>T_{m02}</i> [B]	0.66 s	0.81 s	0.46 s	0.27	X	0.93	0.29	1.18 s	1.35 s	-0.89 s	0.19	X	0.97	0.53
<i>T_{m02}</i> [C]	1.47 s	2.03 s	-0.79 s	0.40	X	0.86	0.29	1.04 s	1.36 s	-0.25 s	0.20	X	0.96	0.91
θ_m [A] ^b	4.7°	6.2°	3.3°	X	X	X	X	7.1°	8.3°	-6.2°	X	X	X	X
θ_m [B]	42.3°	47.2°	-30.3°	X	X	X	X	18.3°	23.8°	-1.6°	X	X	X	X
θ_m [C]	23.3°	28.0°	22.3°	X	X	X	X	X	X	X	X	X	X	X

^a The Nash index only applies to tidal water level calibration/validation.

^b For the wave direction, we do not take into account the following statistics: SI, BSS, and *r*, which involve the angle magnitude

On the other hand, the spectral wave simulation misses several peaks in *H_s*, most notably the calibration for gauge B, and somewhat in the calibration of gauge C. Validation of wave height is performed for the NE monsoon season with higher waves and more consistent directions. Hence, although the absolute error is largest for gauge C validation (RMSE = 33.1 cm), the relative error (SI = 0.25) is smaller than that of gauge B calibration (0.36). All such errors are mainly because the time series of *H_s* varies gradually compared to the observed series. Thus, when considering a long time period in which the positive and negative errors cancel out, the bias is lower (only 9.2 cm), and the BSS is relatively high (≥ 0.88). This has a good implication in estimating the wave power, where the computation is performed for a simulation period ranging from one month to one season.

The calibration and validation result for the wave period (Table 2) show reasonable accuracy except for gauge C, where more energetic waves have been observed. The temporal variability in wave directions is difficult to simulate; the highest RMSE (47.2°) is in the case of gauge B calibration. Again, the validation cases (for the NE monsoon) with more consistent wave directions generally produce smaller errors.

To convince further that the simulations would result in *P* that is not too different from expected, we assume the deep-water condition and apply Eq. (1) for locations A, B, and C using measured and simulated time series of *H_s*. This applies even for an RMSE of *H_s* as large as 33.1 cm, and a scatter index as high as 0.36. The result (not detailed here but included in the supplementary material) shows only a relative difference of +7.0% in *P* for the latter case (validation at C) and +3.5% for the latter case (calibration at B).

V. RESULTS AND DISCUSSION

Each wave condition in Table 1 is specified as a boundary condition for a MIKE21 SW scenario. The modelling is performed in the non-stationary mode, and the wave field quickly reaches equilibrium after six hours of simulation. The wave field output (Fig. 5) is shown for the typical case of NE waves. It is apparent that the wave

model can reproduce important physical processes such as wave refraction and sheltering effect behind islands. The largest wave power at the seaward boundary is > 24 kW/m, while in sheltered bays, this value may reduce to just below 2 kW/m.

From the simulation output, information on the wave power vector **P** can be extracted along the predefined 30-m depth contour using the MIKE21 software package. By taking the projection of vector **P** on the local normal of the depth contour, we can estimate the shoreward magnitude (*P_n*) of this wave power vector:

$$P_n = P \cos \alpha \quad (6)$$

where *P* is the wave power magnitude and α is the

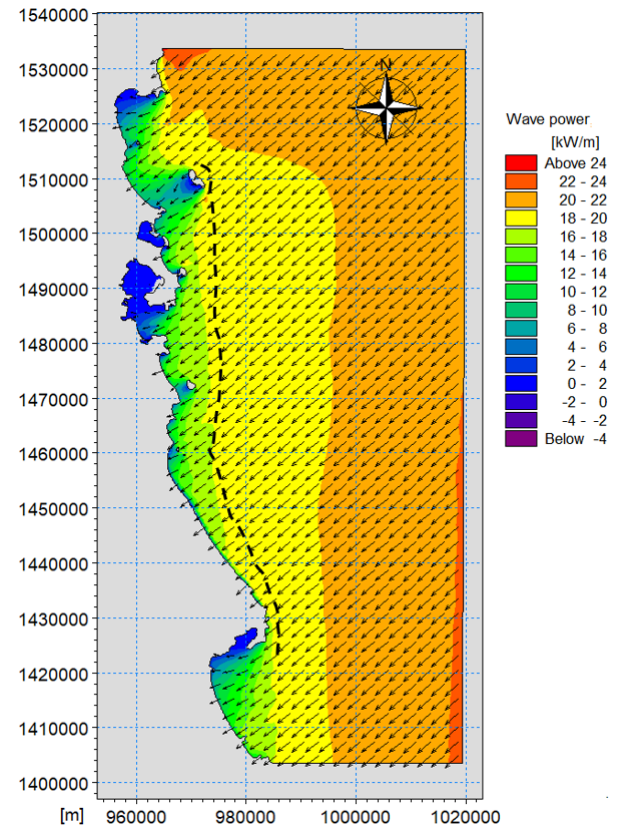


Fig. 5. Wave power field from the simulation for NE waves in January. The 30-m depth contour segment is also shown as a dashed curve.

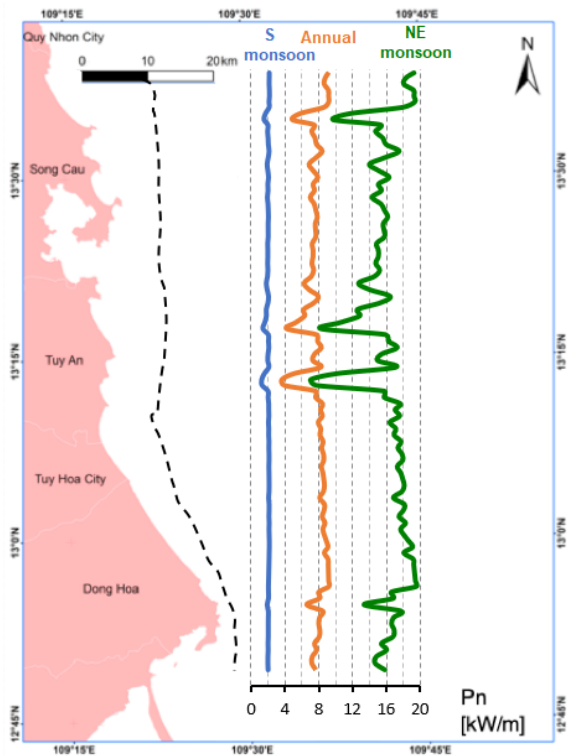


Fig. 6. Distribution of wave power along the 30-m contour depth [dashed curve] of Phu Yen coastline (annually-averaged and seasonally-averaged for S and NE monsoons)

angle between vector \mathbf{P} and the local normal of the 30-m depth contour. Referring to Fig. 5, the wave vectors tend to make an angle of 45° with most parts of the contour, except for the segment corresponding to coordinate $Y = 1430000$ m to 1460000 m, where the wave vectors are almost perpendicular to this contour.

The distributions of time-averaged wave power are shown in Fig. 6. The averaging time periods considered are full-year, NE monsoon season, and S monsoon season. In each distribution, the maximum wave power occurs at the northern side of the Dong Hoa peninsula, where the coast is highly exposed with a steep continental slope and the 30-m contour relatively close to the shoreline, and the NE waves propagating almost perpendicular to the contour. In contrast, the minimum is the northernmost part offshore Tuy An, mainly because the contour line is more aligned with the wave propagation direction. Also, wave power is reduced just north of Song Cau, where the contour swerves around an island (Fig. 5) and thus, the angle between the contour normal and the wave vector is changed locally.

Regarding the annual time scale, P_n varies around 8 kW/m. The computed result reflects a lower average power than the potential deep-water wave power (≥ 25 kW/m) mentioned in the literature [15],[23]. However, this difference is reasonable because the present study has been performed on a localised wave model with a higher resolution, and the orientation of the depth contour is also taken into account when determining wave power. Another study [36] showed that the annual wave power along the Phu Yen coast is only 3.3 kW/m

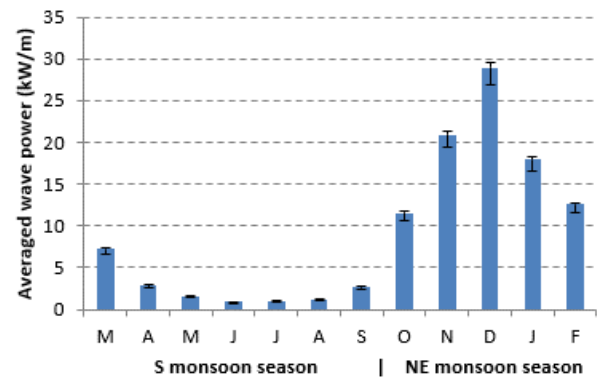


Fig. 7. Monthly wave power, averaged for the entire 30-m contour line. The “error bars” indicate the variation of wave power when the bathymetric contour shifts from 20-m depth (lower bound) to 50-m depth (upper bound).

since this figure corresponds with lower wave heights nearshore.

The value of wave power varies highly between seasons. During winter, with the dominance of NE monsoon, P_n is much higher than that of summer (with S monsoon). Seasonal distributions may provide useful information for WEC operations. However, the average wave power along the coastline is often considered for the long-term purpose of wave energy extraction.

In Fig. 7, the annually averaged P_n is partitioned for different months, based on occurrence data from Table 1. December is the month when the wave power is highest (29.0 kW/m), whereas the wave power is low from May to August. The marked difference in P_n between S and NE monsoon seasons is also shown in this chart. During the seven months (Mar-Sep) when the southern monsoon dominates, P_n only averages 2.44 kW/m, whereas, for five months in NE monsoon season, the averaged P_n is 18.2 kW/m (a 7.4-fold increase). This power excess can partially satisfy the local need for electricity during the dry season, which begins in January.

We also calculate the monthly distribution of wave power for two other cases: the contour is at 20 m depth and at 50 m depth, and results are superimposed on Fig. 7’s chart as error bars. Obviously, the wave power is greater for further offshore locations (i.e., the 50 m contour). However, the change is not remarkable. On average, the wave power at the 20-m contour is 92%, and at the 50-m contour, 102%, of the base case (30-m contour). Therefore, the 30-m contour is an appropriate route to WEC planning which is guaranteed to absorb the potential amount of wave power.

VI. CONCLUSION

The paper presents new findings in the distribution of offshore wave power along a coastal zone of Phu Yen – part of Vietnam’s Central Coast. Unlike previous findings in the literature, which focus on mapping wave energy of the entire South China Sea, this study provides more detailed wave characteristics along the local coastal zone (with a spatial resolution of ~ 1 km). In addition, the

calculation of wave power perpendicular to a predetermined depth contour in this study would give more practical significance in power extraction compared to a scalar value for wave power which is commonly found on maps in the literature. The method can be readily applied to other coastal provinces of Vietnam.

Wave power has been analysed in various time scales (monthly, seasonally and annually) based on a long-term reanalysis wave dataset. This allows us separately to evaluate the contribution of each monsoon wind component (NE or S – which is a typical feature of the local) to wave generation. The wave power generated by the NE monsoon, albeit during a shorter time period (5 months), is 7.4 times higher than that during the dominant period of the S monsoon.

The fully calibrated and validated coupled wave-hydrodynamic model can capture a very detailed wave pattern near the rugged coast of Central Vietnam. Although some observed peaks in wave height were missed in the simulation, we have shown that the error of wave power P as a derived quantity would be lower than that of H_s , and thus the validated wave model is capable of estimating the wave power P_n through the depth contour chosen. The effect of local topography/bathymetry is considered in the simulation. For example, in Fig. 5, the leeward side of islands and rocky peninsulas would notably reduce wave power if devices were not arranged along the 30-m contour depth. This information is essential for effective WEC planning and deployment to extract renewable energy resources in the area.

APPENDIX. METRIC FOR MODEL CALIBRATION AND VALIDATION

The goodness-of-fit between the simulation results and measured data is evaluated based on a set of scores. The Nash index [37] is used only for the flow module. Other scores, including the mean absolute error, the root-mean-square error, the bias, the scatter index, the Brier skill score [38] and the correlation coefficient, are used for both the flow and wave modules. The detailed formulae are:

$$\text{Nash} = 1 - \frac{\sum(x'_i - x_i)^2}{\sum(x_i - \bar{x})^2} \quad (7)$$

$$\text{MAE} = \frac{1}{N} \sum |x'_i - x_i| \quad (8)$$

$$\text{RMSE} = \sqrt{\frac{1}{N} \sum (x'_i - x_i)^2} \quad (9)$$

$$\text{Bias} = \frac{\sum(x'_i - x_i)}{N} \quad (10)$$

$$\text{SI} = \frac{\text{RMSE}}{\bar{x}} \quad (11)$$

$$\text{BSS} = 1 - \frac{\overline{(x'_i - x_i)^2}}{\bar{x}_i^2} \quad (12)$$

$$r = \frac{\sum(x_i - \bar{x})(x'_i - \bar{x}')}{\sqrt{\sum(x_i - \bar{x})^2 \sum(x'_i - \bar{x}')^2}} \quad (13)$$

where MAE is the mean absolute error, RMSE the root-mean-square error, SI the scatter index, r the correlation coefficient, BSS the Brier skill score, x_i the i -th measured value, x'_i the i -th computed value, and \bar{x} the average measured value. The Σ denotes summing over the index i ($i = 1, \dots, N$) where N is the number of values in the data series. When the variable considered is the wave angle ($x = \theta$), the difference is performed with modulus 180° to ensure that this difference does not exceed half a circle.

Supplementary data for calibration, validation and wave power estimation is available from <https://github.com/nguyenquangchien/wave-energy-VN>

REFERENCES

- [1] J. Falnes, J. Løfseth "Ocean wave energy," *Energ Policy* vol. 19, no. 8, pp. 768-775, 1991. DOI: 10.1016/0301-4215(91)90046-Q
- [2] M. Lehmann, F. Karimpour, C.A. Goudey, P.T. Jacobson, M.R. Alam "Ocean wave energy in the United States: current status and future perspectives," *Renew Sust Energ Rev* vol. 74, pp. 1300-1313, 2017. DOI: 10.1016/j.rser.2016.11.101
- [3] D. Khojasteh, S. M. Mousavi, W. Glamore, G. Iglesias "Wave energy status in Asia," *Ocean Eng* vol. 169, pp. 344-358, 2018. DOI: 10.1016/j.oceaneng.2018.09.034
- [4] Wave Dragon ApS, "The Wave Dragon Technology," [Online]. Available: <http://www.wavedragon.net>
- [5] EMEC: European Marine Energy Centre "Pelamis wave power," [Online]. Available: <http://www.emec.org.uk/about-us/wave-clients/pelamis-wave-power>
- [6] J. Twidell, and T. Weir, *Renewable Energy Resources*, 2nd edition. Routledge, UK, 2005
- [7] J. Drew, A. R. Plummer, and M. N. Sahinkaya, "A review of wave energy converter technology," *P I Mech Eng A-J Pow* vol. 223, pp. 887-902, 2009. DOI: 10.1243/09576509JPE782
- [8] T. Aderinto, and H. Li, "Ocean wave energy converters: status and challenges," *Energies* vol. 11, no. 5, pp. 1250, 2017. DOI: 10.3390/en11051250
- [9] R. G. Coe, Y.-H. Yu, J. Van Rij, "A survey of WEC: reliability, survival and design practices," *Energies* vol. 11, no. 1, pp. 4, 2018. DOI: 10.3390/en11010004
- [10] I. Glendenning, "Ocean wave power," *Appl Energ* vol. 3, pp. 197-222, 1977. DOI:10.1016/0306-2619(77)90036-8
- [11] J. M. Leishman, G. Scobie, "The development of wave power – a techno-economic study," Report EAU M25, National Engineering Laboratory UK, 1976. DOI: 10.7488/era/696

- [12] L. Liberti, A. Carillo, G. Sannino, "Wave energy resource assessment in the Mediterranean, the Italian perspective," *Renew Energ* vol. 50, pp. 938-949, 2013. DOI: 10.1016/j.renene.2012.08.023
- [13] B. Aydogan, B. Ayat, and Y. Yuksel, "Black Sea wave energy wave atlas hindcasted wave data," *Renew Energ* vol. 57, pp. 436-447, 2013. DOI: 10.1016/j.renene.2013.01.047
- [14] C. W. Zheng, H. Zhuang, X. Li, and X. Q. Li, "Wind energy and wave energy resources assessment in the East China Sea and South China Sea," *Sci China Technol Sci* vol. 55, no. 1, pp. 163-173, 2012. DOI: 10.1007/s11431-011-4646-z
- [15] N. M. Hung and D. C. Dien, "Research on evaluating the potential of major oceanic energy sources and suggestion on exploitation (in Vietnamese)," Report for research project code KC.09.19/06-10, Hanoi, Vietnam, 2010.
- [16] S. Yang, S. Duan, L. Fan, C. Zheng, X. Li, H. Li, J. Xu, Q. Wang, and M. Feng, "10-year wind and wave energy assessment in the North Indian Ocean," *Energies* vol. 12 no. 20, pp. 10.3390, 2019. DOI: 10.3390/en12203835
- [17] B. Kamranzad and P. Lin, "Sustainability of wave energy resources in the South China Sea based on five decades of changing climate," *Energy* vol. 210:118604, 2020. DOI: 10.1016/j.energy.2020.118604
- [18] E. Rusu, "Study of the wave energy propagation patterns in the Western Black Sea," *Appl Sci* vol. 8: pp. 993, 2018. DOI: 10.3390/app8060993
- [19] S. Behrens, J. Hayward, M. Hemer, and P. Osman, "Assessing the wave energy converter potential for Australian coastal regions," *Renew Energ* vol. 43, pp. 210-217, 2012. DOI: 10.1016/j.renene.2011.11.031
- [20] L. Rusu, and C. Guedes Soares, "Wave energy assessments in the Azores islands," *Renew Energ* vol. 45, pp. 183-196, 2012. DOI: 10.1016/j.renene.2012.02.027
- [21] P. Mota, and J. P. Pinto, "Wave energy potential along the western Portuguese coast," *Renew Energ* vol. 71, pp. 8-17, 2014. DOI: 10.1016/j.renene.2014.02.039
- [22] N. H. Nhat *et al.*, "Research on using ocean wave power for supplying signal buoys offshore Vietnam," Report for the research project – Ministry of Traffic and Transportation, Hanoi, Vietnam, 2002
- [23] D. N. Quynh *et al.*, "Assessment on the potential of Vietnam marine energy," Report for the research project, Vietnam Academy of Science and Technology, Hanoi, 2004
- [24] C. N. Wang, Y. T. Chen, C. C. Tung, "Evaluation of wave energy location by using an integrated MCDM approach," *Energies* vol. 14, pp. 1840, 2021. DOI: 10.3390/en14071840
- [25] Vietnam Meteorological and Hydrological Administration, "Potential of Offshore Marine Renewable Energy for Vietnam", Technical Report (in Vietnamese), 2022.
- [26] NOAA, WaveWatch III Data Access, [Online]. Available: <https://polar.ncep.noaa.gov/waves/download.shtml>
- [27] J.-B. Saulnier, M. Prevosto, and C. Maisondieu, "Refinements of sea state statistics for marine renewables: a case study from simultaneous buoy measurements in Portugal," *Renew Energ* vol. 36, no. 11, pp. 2853-2865, 2011. DOI: 10.1016/j.renene.2011.04.015
- [28] A. Chawla, D. M. Spindler, and H. L. Tolman, "Validation of a thirty year wave hindcast using the Climate Forecast System winds," *Ocean Modell* vol. 70, pp. 189-206, 2013. DOI: 10.1016/j.ocemod.2012.07.005
- [29] H. Karunarithna, P. Maduwantha, B. Kamranzad, H. Rathnasooriya, and K. De Silva, "Impacts of global climate change on the future ocean wave power potential: a case study from the Indian Ocean," *Energies* vol. 13, pp. 3028, 2020. DOI: 10.3390/en13113028
- [30] Y. Goda, *Random Seas and Design of Maritime Structures*, 3rd edition. World Scientific, Singapore, 2010
- [31] DHI, MIKE 21 Flow Model FM. Hydrodynamic Module User Guide, 148 pp, 2017
- [32] Tomidokoro, G., "Basic study on the hydraulic characteristics of the wind-driven currents and dispersion in closed shallow water basins", PhD dissertation, Kyoto University, Japan (in Japanese), 1984.
- [33] Tsanis, I.K., Wu, J., Shen, H., Valeo, C. *Environmental Hydraulics: Hydrodynamics and Pollutant Transport Modelling of Lakes and Coastal Waters*. Elsevier, 2007.
- [34] Roelvink, D. and Reniers, A. *A guide to modeling coastal morphology*. World Scientific.
- [35] Y. Cheng, and O. B. Andersen, "Multimission empirical ocean tide modeling for shallow waters and polar seas," *J Geophys Res - Oceans* vol. 116, no. C11, pp. 007172, 2011. DOI: 10.1029/2011JC007172
- [36] N. N. Thinh, D. V. Nguyen, L. T. Phung, and N. T. Bay, "A study to determine sea wave energy in the South Central Coast," *Vietnam J Hydrometeorol* vol. 722, pp. 58-67, 2021. DOI: 10.36335/VNJHM.2021(722).58-67
- [37] J. E. Nash, J. V. Sutcliffe, "River flow forecasting through conceptual models; part I - a discussion of principles," *J Hydrol* vol. 10, no. 3, pp. 282-290. DOI: 10.1016/0022-1694(70)90255-6
- [38] A. H. Murphy and E. S. Epstein, "Skill scores and correlation coefficients in model verification," *Mon Weather Rev* vol. 117, pp. 572-581, 1989. DOI: 10.1175/1520-0493(1989)117<0572:SSACCI>2.0.CO;2